

# A WENO Algorithm of the Temperature and Ionization Profiles around a Point Source

Jing-Mei Qiu <sup>a</sup>, Long-Long Feng <sup>b,c</sup>, Chi-Wang Shu <sup>a</sup>,  
Li-Zhi Fang <sup>d</sup>

<sup>a</sup>*Division of Applied Mathematics, Brown University, Providence, RI 02912, USA*

<sup>b</sup>*Purple Mountain Observatory, Nanjing, 210008, P.R. China*

<sup>c</sup>*National Astronomical Observatories, Chinese Academy of Science, Chao-Yang District, Beijing 100012, P.R. China*

<sup>d</sup>*Department of Physics, University of Arizona, Tucson, AZ 85721, USA*

---

## Abstract

We develop a numerical solver for radiative transfer problems based on the weighted essentially nonoscillatory (WENO) scheme modified with anti-diffusive flux corrections, in order to solve the temperature and ionization profiles around a point source of photons in the reionization epoch. Algorithms for such simulation must be able to handle the following two features: 1. the sharp profiles of ionization and temperature at the ionizing front (I-front) and the heating front (T-front), and 2. the fraction of neutral hydrogen within the ionized sphere is extremely small due to the stiffness of the rate equations of atom processes. The WENO scheme can properly handle these two features, as it has been shown to have high order of accuracy and good convergence in capturing discontinuities and complicated structures in fluid as well as to be significantly superior over piecewise smooth solutions containing discontinuities. With this algorithm, we show the time-dependence of the preheated shell around a UV photon source. In the first stage the I-front and T-front are coincident, and propagate with almost the speed of light. In later stage, when the frequency spectrum of UV photons is hardened, the speeds of propagation of the ionizing and heating fronts are both significantly less than the speed of light, and the heating front is always beyond the ionizing front. In the spherical shell between the I- and T-fronts, the IGM is heated, while atoms keep almost neutral. The time scale of the preheated shell evolution is dependent on the intensity of the photon source. We also find that the details of the pre-heated shell and the distribution of neutral hydrogen remained in the ionized sphere are actually sensitive to the parameters used. The WENO algorithm can provide stable and robust solutions to study these details.

*Key words:* cosmology: theory, gravitation, hydrodynamics, methods: numerical, shock waves

## 1 Introduction

The profile of HII region around an isolated source of UV photons is an old topic in astrophysics. A classical result was given by Strömgren (1939), who showed that the profile of the spherical HII region of a point source embedded in a uniformly distributed hydrogen gas with number density  $n$  at radial coordinate  $r = 0$  can be approximately described by a step function as

$$f_{\text{HII}}(r) \simeq \theta[R_s - r] = \begin{cases} 1, & \text{if } r < R_s \\ 0, & \text{if } r > R_s \end{cases} \quad (1)$$

where the fraction of ionized hydrogen  $f_{\text{HII}}(r) \equiv n_{\text{HII}}(r)/n$ ,  $n_{\text{HII}}(r)$  being the number density of ionized hydrogen. That is, hydrogen gas is sharply divided into two regions: within a sphere with Strömgren radius  $R_s$  around the source, hydrogen is fully ionized, while outside the sphere hydrogen atoms remain neutral.  $R_s$  is determined by the balance between ionization and recombination

$$R_s = \left( \frac{3\dot{N}}{4\pi\alpha_B n^2} \right)^{1/3}, \quad (2)$$

where  $\dot{N}$  is the emission of ionizing photons of the source, and  $\alpha_B$  is the recombination coefficient of HII (Osterbrock & Ferland 2005). The sharp boundary at  $r = R_s$  is the ionization front (I-front) separating the HII and HI regions.

The problem of the Strömgren sphere has once again attracted many studies recently, because the formation of HII regions around high redshift quasars, galaxies and first stars is crucial to understanding the evolution of the reionization (Cen & Haiman 2000; Madau & Rees 2000; Ciardi et al. 2001; Ricotti et al. 2002; Wyithe & Loeb, 2004; Kitayama, et al. 2004; Whalen et al. 2004; Yu, 2005; Yu & Lu 2005; Alvarez et al. 2006, Iliev et al. 2006). Unlike the static solution eq.(1), new studies focus on the dynamical behavior of the ionized sphere, such as the time-dependence of the ionization profile  $f_{\text{HII}}(t, r)$ , the propagation of the I-front. Besides the HII region and the I-front, a high kinetic temperature region also exists around the UV photon source due to the photon-heating of gas. Similar to the I-front, there is also a T-front separating heated and un-heated gas. The temperature profile  $T(t, r)$  and the T-front are important for probing reionization. For instance, the region with high kinetic temperature  $T$  and low  $f_{\text{HII}}$  would be the 21 cm emission region associated with sources at the reionization epoch (Tozzi et al. 2000; Wyithe

et al. 2005; Cen, 2006; Chen & Miralda-Escude 2006). Although the possible existence of a 21 cm emission shell around high redshift quasars and first stars has been addressed qualitatively or semi-analytically in these references, a serious calculation seems to be still lacking.

Many numerical solvers for the radiative transfer equation have been proposed (Ciardi et al. 2001, Gnedin & Abel 2001, Sokasian et al. 2001, Nakamoto et al. 2001; Razoumov et al. 2002, Cen 2002, Maselli et al. 2003, Shapiro et al., 2004; Rijkhorst et al. 2005; Mellema et al. 2006; Susa 2006, Whalen & Norman 2006). These solvers provide numerical results of the I-front. However, the results are still diverse due to the usage of different approximations. Some of the results show that the time scale of the I-front evolution is sensitively dependent on the intensity of source (White et al. 2003), while some yield intensity-independent evolution (e.g. Mellema et al. 2006). This is because the retardation of photon propagation is ignored in the later, while the recombination is ignored in the former. Therefore, it is worth to re-calculate this problem without above-mentioned assumptions. It has been pointed out that to study the dynamical features of the I- and T-fronts, one would need to apply high-resolution shock-capturing schemes similar to those developed in fluid dynamics (Razoumov & Scott 1999). The finite difference WENO scheme is an algorithm satisfying this requirement.

Moreover, although the fraction of the remained neutral hydrogen within the ionized sphere is extremely small, it is not zero. The small fraction is important to estimate the Ly- $\alpha$  photon leaking at high redshifts. Therefore, a proper algorithm for the dynamical properties of the ionized sphere should be able to, on the one hand, effectively capture sharp profile of ionization and temperature around the I- and T-fronts, and, on the other hand, give a precise value of the remained neutral hydrogen between the discontinuities. This can also be satisfied by the WENO algorithm.

The WENO algorithm has proved to have high order of accuracy and good convergence in capturing discontinuities and complicated structures in fluid as well as to be significantly superior over piecewise smooth solutions containing discontinuities (Shu 2003). We have shown that the WENO algorithm is indeed effective for solving radiative transfer problem with discontinuities with high accuracy. For instance, it can follow the propagation of a sharp I-front and the step function cut-off of retardation (Qiu et al. 2006). We now develop this method to solve both ionization and temperature profiles. It is not a trivial generalization. Because the rate equations of heating-cooling and ionization-recombination are stiff, the time integration of the WENO scheme cannot be directly implemented. A proper strategy to save computational cost on time integration will be developed. A long-term motivation of this work, as we mentioned in (Qiu et al. 2006), is to develop a WENO solver of hydrodynamic/radiative transfer problems, similar to the development of a hybrid

algorithm of hydrodynamic/N-body simulation based on WENO scheme (Feng et al. 2004).

The paper is organized as follows. Section 2 describes the problem and equations needed to be solved. Section 3 presents the WENO numerical scheme. Section 4 gives the solutions of the temperature and ionization profiles and the evolution of energy spectrum of photons. A discussion and conclusion are given in Section 5. Details of the atomic processes are listed in the Appendix.

## 2 Basic Equations

To demonstrate the algorithm, we consider the ionization of a uniformly distributed hydrogen gas in space  $\mathbf{x}$  with number density  $n$  by a point UV photon source located at the center  $|\mathbf{x}| = r = 0$ . Adding helium component in the gas is straightforward and will not change the algorithm for radiative transfer. If the time scale  $t$  of the growth of the ionized sphere is less than  $1/H(t)$ ,  $H(t)$  being the Hubble parameter, the expansion of the universe can be ignored. The radiative transfer equation of the specific intensity  $J(t, r, \nu)$  is then (see the Appendix)

$$\frac{\partial J}{\partial(ct)} + \frac{1}{r^2} \frac{\partial}{\partial r} (r^2 J) = -k_\nu J + S \quad (3)$$

where  $\nu$  is the frequency of photon. The source term,  $S$ , is given by

$$S(t, |\mathbf{x}|, \nu) = \dot{E}(\nu) \delta(\mathbf{x}) \quad (4)$$

where  $\dot{E}(\nu) d\nu$  is the energy distribution of photons emitted by the central source per unit time within the frequency range from  $\nu$  to  $\nu + d\nu$ . We assume the energy spectrum of UV photons to be of a power law  $\dot{E}(\nu) = \dot{E}_0(\nu_0/\nu)^\alpha$ , and  $\nu_0$  is the ionization energy of the ground state of hydrogen  $h\nu_0 = 13.6$  eV. Integration of  $\dot{E}$  over  $\nu$  gives the total intensity (energy per unit time) of ionizing photons emitted by the source,  $\dot{E} = \int_{\nu_0}^{\infty} \dot{E}(\nu) d\nu = \dot{E}_0 \nu_0 / (\alpha - 1)$ .

The absorption coefficient of eq.(3) is  $k_\nu = \sigma(\nu) n_{\text{HI}}(t, \mathbf{x})$ , where the cross section  $\sigma(\nu) \simeq \sigma_0(\nu_0/\nu)^3$  and  $\sigma_0 = 6.3 \times 10^{-18}$  cm<sup>2</sup>. The evolution of the number density of neutral hydrogen HI,  $n_{\text{HI}}(t, r)$ , is governed by the ionization equation,

$$\frac{df_{\text{HI}}}{dt} = \alpha_{\text{HII}} n_e f_{\text{HII}} - \Gamma_{\gamma\text{HI}} f_{\text{HI}} - \Gamma_{\text{eHI}} n_e f_{\text{HI}} \quad (5)$$

where  $f_{\text{HI}} \equiv n_{\text{HI}}(t, r)/n$  is the fraction of neutral hydrogen, and  $n_e$  is the number density of electrons. Obviously,  $f_{\text{HI}}(t, r) + f_{\text{HII}}(t, r) = 1$ . In eq.(5),  $\alpha_{\text{HII}}$  is the recombination coefficient and  $\Gamma_{\text{eHI}}$  is the collision ionization rate.

The photoionization rate  $\Gamma_{\gamma\text{HI}}(t, r)$  is given by

$$\Gamma_{\gamma\text{HI}}(t, r) = \int_{\nu_0}^{\infty} d\nu \frac{J(t, r, \nu)}{h\nu} \sigma(\nu). \quad (6)$$

The kinetic temperature of baryon gas is determined by the equation

$$nk_B \frac{dT}{dt} = H - n^2 C \quad (7)$$

where  $k_B = 1.38 \times 10^{-16}$  erg  $K^{-1}$  is the Boltzmann constant and the temperature  $T$  is in unit of K. The details of the heating  $H$  and cooling  $C$  are given in the Appendix.

### 3 Numerical Algorithm

#### 3.1 Dimensionless variables

In the numerical implementation, it is convenient to introduce the dimensionless variables of time, space and frequency defined by  $t' = c\sigma_0 n t$ ,  $r' = \sigma_0 n r$  and  $\nu' = \nu/\nu_0$ .  $1/\sigma_0 n$  is the optical depth of ionizing photon in neutral hydrogen gas with density  $n$ . Therefore,  $t'$  and  $r'$  are respectively, the time and distance in units of mean free flight time and mean free path of ionizing photon  $h\nu_0$  in the non-ionized background hydrogen gas  $n$ . For the  $\Lambda$ CDM model,  $n = 1.88 \times 10^{-7} (1+z)^3 \text{ cm}^{-3}$ , where  $z$  is redshift,  $t' = 0.89(1+z)^{-3} t$  Myrs and  $r' = 0.27(1+z)^{-3} r$  Mpc. Correspondingly, the intensity is rescaled by  $J d\nu = (1/r^2)(h\nu_0/\sigma_0^3 n) J' d\nu'$ . Thus, eqs.(3), (5), (6) and (7) become

$$\frac{\partial J'}{\partial t'} + \frac{\partial J'}{\partial r'} = - \left( \frac{1}{\nu'} \right)^3 f_{\text{HI}} J', \quad (8)$$

and

$$c\sigma_0 \frac{df_{\text{HI}}}{dt'} = \alpha_{\text{HII}} f_{\text{HII}}^2 - \frac{\Gamma_{\gamma\text{HI}}}{n} f_{\text{HI}} - \Gamma_{\text{eHI}} (1 - f_{\text{HI}}) f_{\text{HI}}. \quad (9)$$

$$\frac{\Gamma_{\gamma\text{HI}}(t, r)}{n} = \frac{1}{r'^2} \int_1^{\infty} d\nu' \frac{J'(t, r, \nu')}{\nu'} \frac{1}{\nu'^3} \quad (10)$$

$$c\sigma_0 k_B \frac{dT}{dt'} = \frac{1}{n^2} H - C. \quad (11)$$

where we have assumed  $n_e/n = f_{\text{HI}}$  and

$$\frac{1}{n^2} H = \frac{h\nu_0}{r'^2} f_{\text{HI}} \int_1^{\infty} \frac{\nu' - 1}{\nu'^4} J' d\nu' \quad (12)$$

The point source condition eq.(4) requires  $\dot{E}(\nu)d\nu = 4\pi(h\nu_0/n\sigma_0^3)J'(t, 0, \nu')d\nu'$ . If we take  $J'(t, 0, \nu') = J_0(1/\nu')^\alpha$ , the total intensity of the source is given by

$$\dot{E} = \frac{4\pi h\nu_0}{(\alpha - 1)n\sigma_0^3}J_0 = 5.8 \times 10^{42} \frac{1}{\alpha - 1} \left( \frac{10}{1 + z_r} \right)^3 \left( \frac{J_0}{10^{-3}} \right) \text{ erg/s.} \quad (13)$$

In our numerical calculation, we solve the system of equations (8), (9) and (11) for the specific intensity  $J'$ , the fraction of the neutral hydrogen  $f_{\text{HI}}$  and the temperature  $T$  as functions of the radius  $r'$ , frequency  $\nu'$  and time  $t'$ . We will drop the prime in the variables  $J'$ ,  $r'$ ,  $\nu'$  and  $t'$  in this section below, when there is no ambiguity, and keep prime in the variables in showing the numerical results.

To solve the radiative transfer equation, we adopt the fifth-order finite difference WENO scheme with anti-diffusive flux corrections. The fifth-order finite difference WENO scheme was designed in (Jiang & Shu 1996) and the anti-diffusive flux corrections to the high order finite difference scheme was designed in (Xu & Shu 2005). The objective of the anti-diffusive flux corrections is to sharpen the contact discontinuities in the numerical solution of the WENO scheme as well as to maintain high order accuracy. A fourth order quadrature formula is used in the computation of integration in equations (10) and (12). The third order TVD Runge-Kutta time discretization is used in time integration for the system of equations (8), (9) and (11). We now describe our numerical algorithm in more detail.

### 3.2 The computational domain

The computational domain is  $(r, \nu) \in [0, r_{max}] \times [1, \nu_{max}]$ , where  $r_{max}$  and  $\nu_{max}$  are chosen such that  $J(r, \nu, t) \approx 0$  for  $r > r_{max}$  or  $\nu > \nu_{max}$ . In our computation,  $r_{max} = 1200$  and  $\nu_{max} = 10^6$ . The computational domain is discretized into a uniform mesh in the  $r$ -direction and into a smooth non-uniform mesh in the  $\nu$ -direction. The uniform mesh in the  $r$ -direction is

$$r_i = i\Delta r \quad \text{with} \quad \Delta r = r_{max}/N_r, \quad i = 0, \dots, N_r$$

and the non-uniform mesh in the  $\nu$ -direction is taken to be

$$\nu_j = 2^{\xi_j} \quad \text{with} \quad \xi_j = j\Delta\xi, \quad \Delta\xi = \log_2\nu_{max}/N_\nu, \quad j = 0, \dots, N_\nu$$

which is allowed because only integration, e.g. in equations (10) and (12), is involved in the computation with respect to the  $\nu$ -variable. In our model, large  $\nu$  contributes little in equations (10) and (12), therefore the non-uniform mesh is designed in a way such that the mesh becomes coarser for larger  $\nu$ .

### 3.3 Approximation to the spatial derivative

To approximate the spatial derivative in equation (8), the WENO scheme with anti-diffusive flux corrections is used. Specifically, to calculate  $\partial J/\partial r$ , the variable  $\nu$  is fixed and the approximation is performed along the  $r$ -line

$$\frac{\partial}{\partial r} J(t^n, r_i, \nu_j) \approx \frac{1}{\Delta r} (\hat{h}_{i+1/2}^a - \hat{h}_{i-1/2}^a) \quad (14)$$

where the numerical flux  $\hat{h}_{i+1/2}^a$  is obtained with the procedure given below. We can use the upwind fluxes without flux splitting in the fifth order WENO approximation because the wind direction is fixed (positive). To obtain the sharp resolution of the contact discontinuities, the anti-diffusive flux corrections are used in our code.

First, we denote

$$h_i = J(t^n, r_i, \nu_j), \quad i = -2, -1, \dots, N_r + 2$$

where  $n$  and  $j$  are fixed. The numerical flux from the regular WENO procedure is obtained by

$$\hat{h}_{i+1/2}^- = \omega_1 \hat{h}_{i+1/2}^{(1)} + \omega_2 \hat{h}_{i+1/2}^{(2)} + \omega_3 \hat{h}_{i+1/2}^{(3)}$$

where  $\hat{h}_{i+1/2}^{(m)}$  are the three third order fluxes on three different stencils given by

$$\begin{aligned} \hat{h}_{i+1/2}^{(1)} &= \frac{1}{3} h_{i-2} - \frac{7}{6} h_{i-1} + \frac{11}{6} h_i, \\ \hat{h}_{i+1/2}^{(2)} &= -\frac{1}{6} h_{i-1} + \frac{5}{6} h_i + \frac{1}{3} h_{i+1}, \\ \hat{h}_{i+1/2}^{(3)} &= \frac{1}{3} h_i + \frac{5}{6} h_{i+1} - \frac{1}{6} h_{i+2}, \end{aligned}$$

and the nonlinear weights  $\omega_m$  are given by

$$\omega_m = \frac{\tilde{\omega}_m}{\sum_{l=1}^3 \tilde{\omega}_l}, \quad \tilde{\omega}_l = \frac{\gamma_l}{(\varepsilon + \beta_l)^2},$$

with the linear weights  $\gamma_l$  given by

$$\gamma_1 = \frac{1}{10}, \quad \gamma_2 = \frac{3}{5}, \quad \gamma_3 = \frac{3}{10},$$

and the smoothness indicators  $\beta_l$  given by

$$\begin{aligned}
\beta_1 &= \frac{13}{12} (h_{i-2} - 2h_{i-1} + h_i)^2 + \frac{1}{4} (h_{i-2} - 4h_{i-1} + 3h_i)^2 \\
\beta_2 &= \frac{13}{12} (h_{i-1} - 2h_i + h_{i+1})^2 + \frac{1}{4} (h_{i-1} - h_{i+1})^2 \\
\beta_3 &= \frac{13}{12} (h_i - 2h_{i+1} + h_{i+2})^2 + \frac{1}{4} (3h_i - 4h_{i+1} + h_{i+2})^2.
\end{aligned}$$

$\varepsilon$  is a parameter to avoid the denominator to become 0 and is taken as  $\varepsilon = 10^{-5}$  times the maximum magnitude of the initial condition  $J$  in the computation of this paper. The reconstruction of the finite difference WENO flux on the downwind side  $\hat{h}_{i+1/2}^+$  is obtained in a mirror symmetric fashion with respect to  $x_{i+1/2}$  as that for  $\hat{h}_{i+1/2}^-$ .

The anti-diffusive flux corrections are based on the fluxes obtained from the regular WENO procedure. It is given by

$$\begin{aligned}
\hat{h}_{i+1/2}^a &= \hat{h}_{i+1/2}^- + \\
&\phi_i \text{minmod} \left( \frac{h_i - h_{i-1}}{\eta} + \hat{h}_{i-1/2}^- - \hat{h}_{i+1/2}^-, \hat{h}_{i+1/2}^+ - \hat{h}_{i+1/2}^- \right),
\end{aligned} \tag{15}$$

where  $\eta = \Delta t / \Delta r$  is the CFL number and the minmod function is defined as

$$\text{minmod}(a, b) = \begin{cases} 0, & \text{if } ab \leq 0 \\ a, & \text{if } ab > 0, |a| \leq |b| \\ b, & \text{if } ab > 0, |b| < |a|. \end{cases} \tag{16}$$

$\phi_i$  in eq.(15) is the discontinuity indicator between 0 and 1, defined as

$$\phi_i = \frac{\beta_i}{\beta_i + \gamma_i},$$

where

$$\beta_i = \left( \frac{\alpha_i}{\alpha_{i-1}} + \frac{\alpha_{i+1}}{\alpha_{i+2}} \right)^2, \quad \gamma_i = \frac{|u_{\max} - u_{\min}|^2}{\alpha_i}, \quad \alpha_i = (|h_{i-1} - h_i| + \zeta)^2,$$

with  $\zeta$  being a small positive number taken as  $10^{-6}$  in our computation.  $u_{\max}$  and  $u_{\min}$  are the maximum and minimum values of  $h_i$  for all grid points. With the definition above, we will have  $0 \leq \phi_i \leq 1$ .  $\phi_i = O(\Delta r^2)$  in the smooth regions and  $\phi_i$  is close to 1 near strong discontinuities. The purpose of the anti-diffusive flux corrections is to improve the resolution of contact discontinuities without sacrificing accuracy and stability of the original WENO scheme.



### 3.4 High order numerical integration in $\nu$

The integration in equations (10) and (12) is approximated by a fourth order quadrature formula

$$\int_{\nu_0}^{\infty} f(x)dx = \Delta x \sum_{j=j_0}^{\infty} w_j f(j\Delta x) + O(\Delta x^4) \quad (17)$$

where  $\nu_0 = j_0\Delta x$ , and the weights  $w_j$  are given by

$$w_{j_0} = \frac{3}{8}, \quad w_{j_0+1} = \frac{7}{6}, \quad w_{j_0+2} = \frac{23}{24}, \quad w_{j_0+j} = 1, \quad \text{for } j > 2.$$

Again we refer to (Qiu et al. 2006) for details of implementation.

### 3.5 Time integration

When considering the time integration for the system of equations (8), (9) and (11), we start with the third order TVD Runge-Kutta time discretization in (Shu & Osher 1988). For the system of ODEs  $u_t = L(u)$  this time discretization reads

$$u^{(1)} = u^n + \Delta t L(u^n, t^n) \quad (18)$$

$$u^{(2)} = \frac{3}{4}u^n + \frac{1}{4}(u^{(1)} + \Delta t L(u^{(1)})) \quad (19)$$

$$u^{n+1} = \frac{1}{3}u^n + \frac{2}{3}(u^{(2)} + \Delta t L(u^{(2)})) \quad (20)$$

The Runge-Kutta method needs to be modified considering the modification on the anti-diffusive flux  $\hat{f}^a$  by

$$J^{(1)} = J^n + \Delta t L(J^n, t^n) \quad (21)$$

$$J^{(2)} = J^n + \frac{1}{4}\Delta t L'(J^n) + \frac{1}{4}\Delta t L(J^{(1)}) \quad (22)$$

$$J^{n+1} = J^n + \frac{1}{6}\Delta t L''(J^n) + \frac{1}{6}\Delta t L(J^{(1)}) + \frac{2}{3}\Delta t L(J^{(2)}) \quad (23)$$

where the spatial derivative  $\partial J/\partial r$  term in operator  $L$  is defined by (14) with the anti-diffusive flux  $\hat{h}^a$  given by eq.(15), and  $\partial J/\partial r$  in the operator  $L'$  is

defined by the modified anti-diffusive flux  $\bar{h}^a$  as

$$\bar{h}_{i+1/2}^a = \begin{cases} \hat{h}_{i+1/2}^- + \min\left(\frac{4(h_i - h_{i-1})}{\eta}, \hat{h}_{i-1/2}^- - \hat{h}_{i+1/2}^-, \hat{h}_{i+1/2}^+ - \hat{h}_{i+1/2}^- \right), & \text{if } bc > 0, |b| < |c|, \\ \hat{h}_{i+1/2}^a, & \text{otherwise} \end{cases}, \quad (24)$$

and  $\partial J / \partial r$  in the operator  $L''$  is defined by the modified anti-diffusive flux  $\tilde{h}^a$ ,

$$\tilde{h}_{i+1/2}^a = \begin{cases} \hat{h}_{i+1/2}^- + \min\left(\frac{6(h_i - h_{i-1})}{\eta}, \hat{h}_{i-1/2}^- - \hat{h}_{i+1/2}^-, \hat{h}_{i+1/2}^+ - \hat{h}_{i+1/2}^- \right), & \text{if } bc > 0, |b| < |c|, \\ \hat{h}_{i+1/2}^a, & \text{otherwise} \end{cases}, \quad (25)$$

Here  $b = (h_i - h_{i-1})/\eta + \hat{h}_{i-1/2}^- - \hat{h}_{i+1/2}^-$ ,  $c = \hat{h}_{i+1/2}^+ - \hat{h}_{i+1/2}^-$ .

The difficulty of a direct implementation of the scheme lies in the stiffness of equations (9) and (11). Especially for strong sources, when  $J(r=0)$  is large, one needs very small time step  $\Delta t$  to guarantee the stability of the numerical scheme, therefore huge computational cost for long time integration.

By observing that

- Though (9) and (11) are stiff ODEs, (8) involving the spatial derivative is not a stiff equation.
- The WENO procedure with the anti-diffusive flux corrections in approximating the spatial derivative is the major cost at each time step.
- Implicit numerical method in time evolution has milder time step restriction than the explicit one.

we have settled down with the following strategies to save the computational cost

- We use different time scales to solve  $J$  in (8) and to solve  $f_{HI}$  and  $T$  in (9) and (11). The time step for  $J$ , say  $\Delta t$ , is larger, while the time step for  $f_{HI}$  and  $T$ , say  $\delta t = \frac{\Delta t}{N_t}$  with  $N_t$  being the number of small time steps in a large time step, is much smaller. By doing this, we take advantage of the non-stiffness of (8) and eliminate the cost of the WENO procedure with flux corrections for each small time step.
- In each small time step  $\delta t$ , we use a semi-implicit numerical method for strong sources to proceed in time for  $f_{HI}$  and  $T$ , which greatly releases the

severe time step restriction for the sake of the stability of the scheme. The number of small time steps  $\delta t$  in one large time step  $\Delta t$  is thus greatly reduced, hence the saving of the computational cost.

More precisely, we modify the third order TVD Runge-Kutta time discretization in the following procedure

- (1) We have the initial condition of  $J$ ,  $f_{HI}$  and  $T$  at  $t=0$ . Let us denote

$$J^0 = (J_{i,j}^0)_{N_r \times N_\nu} = (J(x_i, \nu_j, t = 0))_{N_r \times N_\nu},$$

$$f_{HI}^0 = (f_{HIi}^0)_{N_r \times 1} = (f_{HI}^0(x_i, t = 0))_{N_r \times 1}; \quad T^0 = (T_i^0)_{N_r \times 1} = (T(x_i, t = 0))_{N_r \times 1}.$$

- (2) For a large time step  $\Delta t$ , we evolve  $J^n$ ,  $f_{HI}^n$  and  $T^n$  by three inner stages to  $J^{n+1}$ ,  $f_{HI}^{n+1}$  and  $T^{n+1}$ .

- $J^{n+1}$ :  
 $J^{(1)}$ ,  $J^{(2)}$ ,  $J^{n+1}$  are updated according to (21), (22), (23).
- $f_{HI}^{n+1}$ ,  $T^{n+1}$ :  
 Let us denote

$$\bar{h} = (h_1, h_2) = (f_{HI}, T)$$

and

$$\begin{aligned} \bar{L}(J, f_{HI}, T) &= (L_1(J, f_{HI}, T), L_2(J, f_{HI}, T)) \\ &= \left( \frac{1}{c\sigma_0} \{ rhs \text{ of (9)} \}, \frac{1}{c\sigma_0 k_B} \{ rhs \text{ of (11)} \} \right) \end{aligned}$$

Instead of (18),  $f_{HI}^{(1)}$  and  $T^{(1)}$  are evolved by

$$(f_{HI}^{(1)}, T^{(1)}) = \bar{h}_{(N_t)}$$

where  $\bar{h}_{(N_t)}$  is the evolution of the solution by the Euler-forward method for  $N_t$  times, with the Euler-forward method at each time step defined as

$$\bar{h}_{(j+1)} = \bar{h}_{(j)} + \delta t \bar{L}(J^n, \bar{h}_{(j)}); \quad (26)$$

Instead of (19), the second inner stage  $\bar{h}^{(2)} = (f_{HI}^{(2)}, T^{(2)})$  is updated by

$$\bar{h}^{(2)} = \frac{3}{4} \bar{h}^n + \frac{1}{4} \bar{h}^{(2')}$$

with  $\bar{h}^{(2')} = \bar{h}_{(N_t)}$  being the evolution of the solution by the Euler-forward method for  $N_t$  times based on  $J^{(1)}$  as

$$\bar{h}_{(j+1)} = \bar{h}_{(j)} + \delta t \bar{L}(J^{(1)}, \bar{h}_{(j)}); \quad (27)$$

Finally, instead of (20),  $f_{HI}^{n+1}$  and  $T^{n+1}$  are computed as

$$\bar{h}^{n+1} = \frac{1}{3} \bar{h}^n + \frac{2}{3} \bar{h}^{(3')}$$

with  $\bar{h}^{(3')} = \bar{h}_{(N_t)}$  obtained in a similar manner as in the previous step but based on  $J^{(2)}$

$$\bar{h}_{(j+1)} = \bar{h}_{(j)} + \delta t \bar{L}(J^{(2)}, \bar{h}_{(j)}). \quad (28)$$

- (3) When the source is strong, (9) and (11) suffer from severe time step restriction, we use a semi-implicit scheme instead of (26) in our code to release the severe time step restriction and to save computational cost. The procedure of the implementation is the same as described above except that (26) is replaced by

$$f_{HI(j+1)} = f_{HI(j)} + \delta t L_1(J^n, f_{HI(j+1)}, T_{(j)}) \quad (29)$$

$$T_{(j+1)} = T_{(j)} + \delta t L_2(J^n, f_{HI(j+1)}, T_{(j+1)}) \quad (30)$$

(29) is computed by solving a quadratic equation with the root located between 0 and 1, since  $L_1$  is a quadratic function of  $f_{HI}$ , and (30) is computed by the Newton iteration method. (27) and (28) are modified in a similar way as (26).

### 3.6 Boundary conditions

The boundary conditions are implemented as follows

- Inflow boundary condition at  $r=0$ :  
 $J_{i,j} = J_{0,j}, \quad \text{for } i = 0, -1, -2.$
- The boundary condition at  $r = r_{max}$ :  
 $J_{N_r+i,j} = J_{N_r-1,j}, \quad \text{for } i = 0, 1, 2$

### 3.7 Convergence study of the numerical scheme

In this subsection, we perform a grid refinement convergence study for the numerical scheme we proposed above, to assess the accuracy of the computational result for the typical mesh sizes that we will use in next section.

We test our numerical schemes for the case with the strongest source intensity, i.e.  $\dot{E} = 5.8 \times 10^{45} \text{ erg s}^{-1}$ . This is the toughest situation for our numerical simulation, as the scheme suffers severe time step restriction due to the stiffness of the ODE. We use both the multi-time-scale strategy and semi-implicit time discretization described in the previous subsections, and compare the results obtained with 4000 points in  $r$  and 200 points in  $\nu$ , which is the typical mesh size used in next section, and with a *coarser* mesh consisting of 2400 points in  $r$  and 100 points in  $\nu$ , in Figure 1. The results with these two mesh sizes

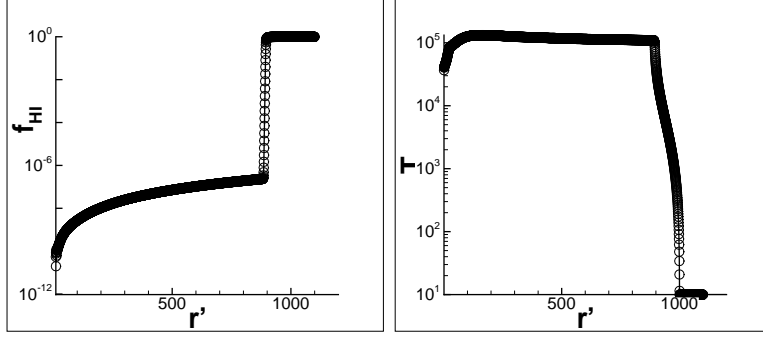


Fig. 1. The profiles of  $f_{\text{HI}}(t, r')$  (left) and  $T(t, r')$  (right) with the source of  $5.8 \times 10^{45}$  erg s $^{-1}$  at time  $t = 0.89$  Myrs ( $t' = 1000$ ). The power-law frequency spectrum has the index  $\alpha = 2$ , and the reionization redshift is taken to be  $1 + z = 10$ . The solid line is the numerical result with the typical mesh  $N_r = 4000$ ,  $N_\nu = 200$ , and the circles indicate the numerical result with a coarser mesh  $N_r = 2400$ ,  $N_\nu = 100$ .

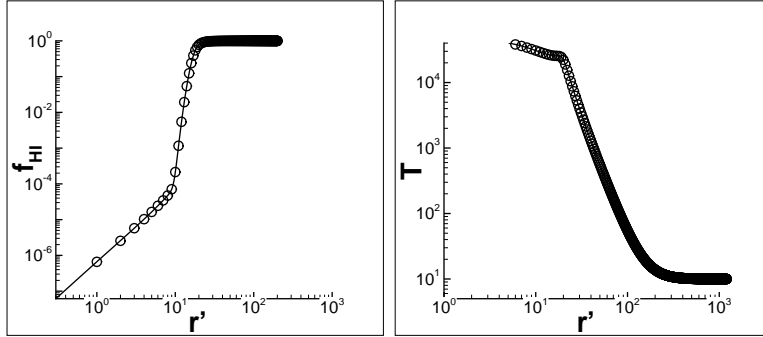


Fig. 2. The profiles of  $f_{\text{HI}}(t, r')$  (left) and  $T(t, r')$  (right) with the source of  $5.8 \times 10^{39}$  erg s $^{-1}$  at time  $t = 0.09$  Myrs ( $t' = 100$ ). The power-law frequency spectrum has the index  $\alpha = 2$ , and the redshift is taken to be  $1 + z = 10$ . The numerical mesh is  $N_r = 2400$  and  $N_\nu = 200$ . The solid line is the numerical solution with single, extremely small time step, and the circles indicate the numerical solution with the multi-time-scale strategy.

match very well, indicating that our numerical results are already numerically convergent at the coarser mesh. The numerical results reported in next section with the finer mesh should therefore be reliable.

We also test the accuracy of our multi-time-scale strategy by comparing the numerical results of evolving (8), (9) and (11) together with single, extremely small time step, and that of updating (8), (9) and (11) by the multi-time-scale strategy with  $(\delta t, \Delta t)$ . These two approaches produce numerical solutions in good agreement, see Figure 2.

Additional grid refinement study, not reported here to save space, has been performed to assure the numerical convergence of the results reported in next section.

## 4 Results

The results in this section are obtained with the numerical algorithm described in the previous section. The code is stable for all the cases reported in this section. As indicated in the previous section 3.7, and we have performed grid refinement study for some representative examples to ensure that the results reported are numerically converged solutions.

In our calculation, we use the explicit time discretization to solve (9) and (11) when  $\dot{E} = 5.8 \times 10^{39} \text{ erg s}^{-1}$ , and semi-implicit scheme when  $\dot{E} = 5.8 \times 10^{41} \text{ erg s}^{-1}$ ,  $5.8 \times 10^{43} \text{ erg s}^{-1}$  and  $5.8 \times 10^{45} \text{ erg s}^{-1}$  in each of the small time step  $\delta t$  in the multi-time-scale strategy.

### 4.1 Profiles of $f_{\text{HI}}(t, r)$ and $T(t, r)$

We calculate the profiles of  $T(t, r)$  and  $f_{\text{HI}}(t, r)$  around a point source. The result is presented in Figure 3, which shows the time-dependence of the profiles  $f_{\text{HI}}(t, r)$  and  $T(t, r)$  for sources with intensity, respectively from top to bottom panels,  $\dot{E} = 5.8 \times 10^{39}$ ,  $5.8 \times 10^{41}$ ,  $5.8 \times 10^{43}$  and  $5.8 \times 10^{45} \text{ erg s}^{-1}$  with  $\alpha = 2$  and  $1 + z = 10$ . The emission rate of the number of photons is roughly  $\dot{N} \simeq 10^{50}$ ,  $10^{52}$ ,  $10^{54}$  and  $10^{56} \text{ s}^{-1}$ .

Figure 3 shows that the ionized sphere generally has a sharp I-front. The time-dependent profile  $f_{\text{HI}}(t, r)$  may still be approximately described as a Strömgen sphere with time-dependent size  $R(t)$  as

$$f_{\text{HI}}(t, r) = \begin{cases} 1, & r > R(t), \\ \simeq 0, & r < R(t) \end{cases} \quad (31)$$

The code can well reveal the propagation of the I-front  $r = R(t)$ . Unlike the solution eq.(1),  $f_{\text{HI}}(t, r)$  is not zero in  $r < R(t)$ . Although the neutral hydrogen  $f_{\text{HI}}(t, r)$  remained in  $r < R(t)$  is very small, it cannot be ignored, because the heating of gas is given by the hard photons absorption of neutral hydrogen HI [eq.(A8)]. The high temperature within the ionized sphere is actually maintained by the ionization of the small fraction therein by all the ionizing photons [eq.(31)]. Figure 3 indicates that  $f_{\text{HI}}(t, r)$  within  $r < R(t)$  is sensitive to the intensity of the source. This is important for investigating leakage of the Ly- $\alpha$  photon.

Figure 3 shows that the temperature profiles  $T(t, r)$  within the I-front  $r < R(t)$  are simple. The temperature keeps around a constant  $10^4 - 10^5 \text{ K}$ . An interesting feature is that for strong sources, the temperature at the center

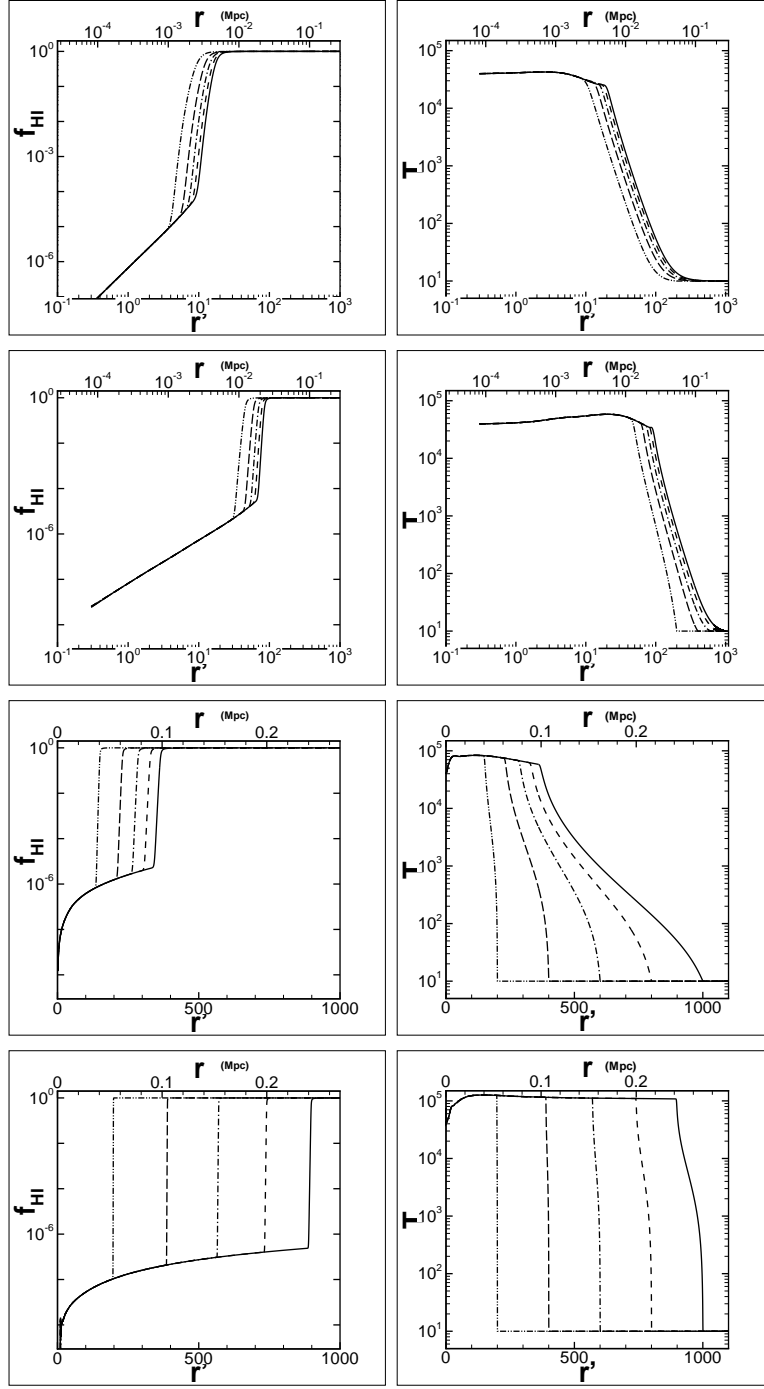


Fig. 3. The profiles of  $f_{\text{HI}}(t, r)$  (left) and  $T(t, r)$  (right), in which  $r$  and  $r'$  are the physical and dimensionless distance, respectively. From top to bottom: for sources of  $\dot{E} = 5.8 \times 10^{39}$ ,  $5.8 \times 10^{41}$ ,  $5.8 \times 10^{43}$  and  $5.8 \times 10^{45}$  erg s $^{-1}$  at time  $t = 0.18$  (dash dot dot), 0.36 (long dash), 0.53 (dash dot), 0.71 (dash), and 0.89 (solid line) Myrs. The power-law frequency spectrum has the index  $\alpha = 2$ , and the redshift is taken to be  $1 + z = 10$ . The mesh has  $N_r=4000$ ,  $N_\nu=200$  grid points.

( $r \approx 0$ ) is not the highest and is even lower than the constant temperature. This is because the ionizing (soft) photon flux at the center is very strong, the number of  $f_{\text{HI}}(r \sim 0)$  is extremely low (see Figure 3), and then, the heating rate is lower.

A common feature of  $T(t, r)$  is that the size of heated region is generally larger than that of ionized region at all time. That is, hydrogen gas is already significantly heated before being ionized. The gas is firstly heated up, and then ionized. The region between the T-front and the I-front is a pre-heating layer, in which the temperature can be as high as  $T \simeq 10^3$  K, or even larger. For a source of  $\dot{E} = 10^{43}$  erg s $^{-1}$  at  $(1+z) = 10$ , the physical size of the ionized region at time 0.36 Mys is about 0.06 Mpc, while the physical size of the region with temperature larger than  $10^3$  K is about 0.08 Mpc. When  $t = 0.89$  Mys, the two physical sizes are, respectively, about 0.1 Mpc, and 0.16 Mpc, or comoving size 1 Mpc, and 1.6 Mpc. Therefore, for strong sources, the time scales and comoving length scales of the pre-heating layer are in the range of cosmological interest.

An important feature of the ionization profile is that  $f_{\text{HI}}(t, r)$  can be approximately written as  $f_{\text{HI}}(t, r) = f_{\text{HI}}(r)\theta[r - R(t)]$ , where  $f_{\text{HI}}(r)$  is time-independent, and  $R(t)$  is only a function of  $t$ . That is, all the time-dependence of  $f_{\text{HI}}(t, r)$  can be described by the I-front  $R(t)$ . In the region  $r < R(t)$ , the ionization profile  $f_{\text{HI}}(t, r) = f_{\text{HI}}(r)$  is time-independent. It can be given by a static or stationary solution of the radiative transfer equation. This property has been applied in some codes for radiative transfer, in which the ionization field is given by the static solution of the radiative transfer equation for a given matter distribution.

For the temperature profile, one might also approximately define a T-front function by a step function as  $\theta[t - R(t, T)]$ . However, unlike the I-front, the temperature profile can not be rewritten as  $T(t, r) = T(r)\theta[t - R(t, T)]$ , where  $T(r)$  is time-independent. That is, the  $r$ -dependence of the function  $T(t, r)$  can not be separated with  $t$ . Especially, the function  $T(t, r)$  in the range between the I- and T-fronts actually always depends strongly on  $t$ .

#### 4.2 Speed of the I- and T-fronts

Figure 3 shows that, for a very strong source  $\dot{E} = 10^{45}$  erg s $^{-1}$ , we have  $R(t) \simeq ct$ , i.e. the ionizing front moves with a speed close to the speed of light. For a weak source  $\dot{E} = 10^{38}$  erg s $^{-1}$ , the profile  $f_{\text{HI}}(t, r)$  does not show a significant expansion of the I-front if time  $t$  is larger than a few of free flight times of ionizing photons. This result is also evident in Figure 4 on  $r_{90}(t)$  versus  $t$ .  $r_{90}(t)$  is defined by  $f_{\text{HI}}(t, r_{90}) = 0.90$ . It denotes the size, within



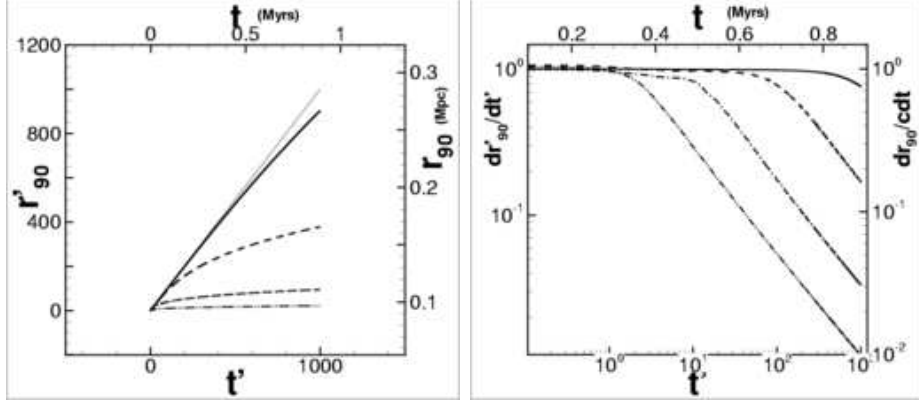


Fig. 4. left panel: the evolution of  $r_{90}(t)$ , which is the solution of  $f_{\text{HI}}(t, r_{90}) = 0.90$ . The light solid line is  $r_{90} = ct$ . Right panel:  $dr_{90}/dt$  vs.  $t$ . Other parameters and the mesh in the numerical simulation are the same as those in Figure 3. The sources are taken to be  $\dot{E} = 5.8 \times 10^{39}$  (dash dot dot),  $5.8 \times 10^{41}$  (dash dot),  $5.8 \times 10^{43}$  (dash), and  $5.8 \times 10^{45}$  (solid line)  $\text{erg s}^{-1}$ . Time  $t'$  is dimensionless.

which, i.e.  $r < r_{90}$ , 90% hydrogen are ionized. Therefore, it can be used for the I-front. For a strong source, such as  $\dot{E} = 10^{45}$   $\text{ergs s}^{-1}$ , we have approximately  $r_{90} = ct$ , which implies that the ionizing region grows with an ionizing front propagating with almost the speed of light. For weak sources,  $r_{90}(t)$  are also following  $t$  at very small  $t$ , but become  $r_{90}(t) < ct$  when  $t$  is large. The weaker the sources, the earlier the stage of  $r_{90}(t) < ct$  takes place. This point is more clearly shown in the right panel of Figure 4. We see that the speed  $dr_{90}(t)/dt$  is close to  $c$  when  $t$  is small, and then the speed decreases with  $t$  by a power law  $dr_{90}(t)/dt \propto t^{-\beta}$  with  $\beta > 2/3$ . One can define a time  $t_i$ , larger than which, the speed  $dr_{90}(t)/dt$  starts to decrease with  $t$  by the power law. At time  $t > t_i$ , the ionizing sphere is still expanding, but very slowly. It will finally approach a solution, of which the ionization equilibrium is approximately established, and the ionized sphere becomes time-independent. The time  $t_i$  depends on the source intensity. The stronger the source, the larger the time  $t_i$ .

Obviously, the speed of the propagation of T-front cannot be larger than the speed of light, and therefore, the T-front will approximately coincide with the I-front when  $t < t_i$ . Only in this period, the ionized sphere is the same as the heated sphere. When  $t > t_i$ , the T-front starts to exceed the I-front, and the pre-heating layer is formed. Therefore, the formation of pre-heated layer happens later for a stronger source.

Figure 5 gives a comparison of  $f_{\text{HI}}(t, r)$  and  $T(t, r)$  at time  $t = 0.89$  Myrs for sources with different intensity. We can see that the pre-heating layer has been well established at time  $t = 0.89$  Myrs for all sources with  $\dot{E} \leq 10^{43}$   $\text{erg s}^{-1}$ , while the T-front of the source with  $\dot{E} = 10^{45}$   $\text{erg s}^{-1}$  is still about the same as the I-front. One can expect that for a source of  $\dot{E} \geq 10^{45}$   $\text{erg s}^{-1}$ , a preheated layer will be formed at time  $t > 0.89$  Myrs and on comoving distance  $r > 2.7$

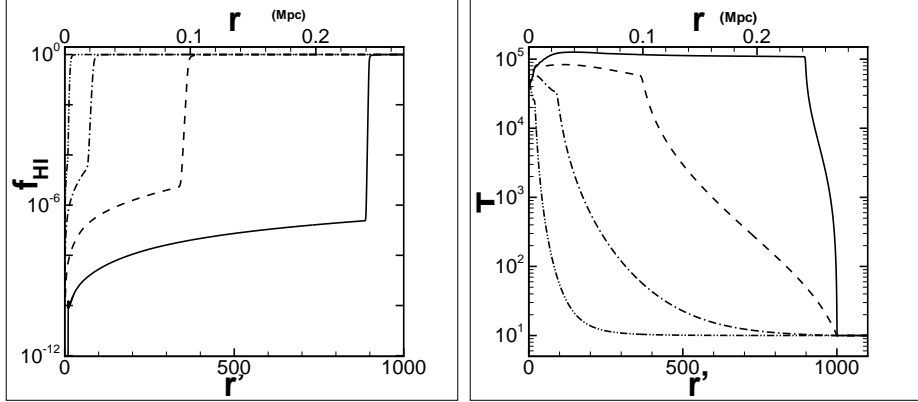


Fig. 5. Profiles of  $f_{\text{HI}}(r)$  (left panel) and  $T(r)$  (right panel) at time  $t = 0.89$  Myrs for sources with intensity  $\dot{E} = 5.8 \times 10^{39}$  (dash dot dot),  $5.8 \times 10^{41}$  (dash dot),  $5.8 \times 10^{43}$  (dash), and  $5.8 \times 10^{45}$  (solid line)  $\text{erg s}^{-1}$ .  $r$  and  $r'$  are the physical and dimensionless distance, respectively. The power-law frequency spectrum has index  $\alpha = 2$ . The redshift is taken to be  $1 + z = 10$ . The mesh in the numerical simulation is the same as that in Figure 3.

Mpc from the source.

### 4.3 Spectral hardening

The formation of the pre-heated layer with high  $T$  and high  $f_{\text{HI}}$  is due to the lack of soft photons beyond the I-front, while hard photons are still abundant in that region. In other words, the energy spectrum of the photons is significantly hardened around the I-front. We now directly demonstrate the evolution of the photon frequency spectrum, as our code can effectively reveal the evolution of radiations in the  $\nu$ -space.

The left panel of Figure 6 gives the frequency spectra of 1.) source  $\dot{E} = 5.8 \times 10^{43}$   $\text{erg s}^{-1}$  at time  $t = 0.89$  Myrs and physical distance  $r = 0.08$ ,  $0.11$ , and  $0.14$  Mpc, and 2.) source  $\dot{E} = 5.8 \times 10^{45}$   $\text{erg s}^{-1}$  at time  $t = 0.89$  Myrs and physical distance  $r = 0.19$  and  $0.24$  Mpc. We can see a significant  $r$ -dependence of the frequency spectrum. At a small  $r$  the spectra are still almost the same as the original power-law spectrum  $\nu^{-\alpha}$  with  $\alpha = 2$ , while at large  $r$ , they significantly deviate from the original power-law. All photons of  $\nu < 10\nu_0$ , are exhausted within  $r < 0.24$  Mpc. At high frequency  $\nu > 50\nu_0$ , the spectra are still of power-law with  $\alpha = 2$ , while at  $\nu < 50\nu_0$  they are substantially dropped. It shows a peak at  $1 < \nu/\nu_0 < 10$ , and looks like a spectrum with self-absorption. However, unlike a self-absorption spectrum, the position of the peak is not fixed in the frequency-space, it moves to higher frequency with time. Namely, the photon energy spectrum is harder at later time.

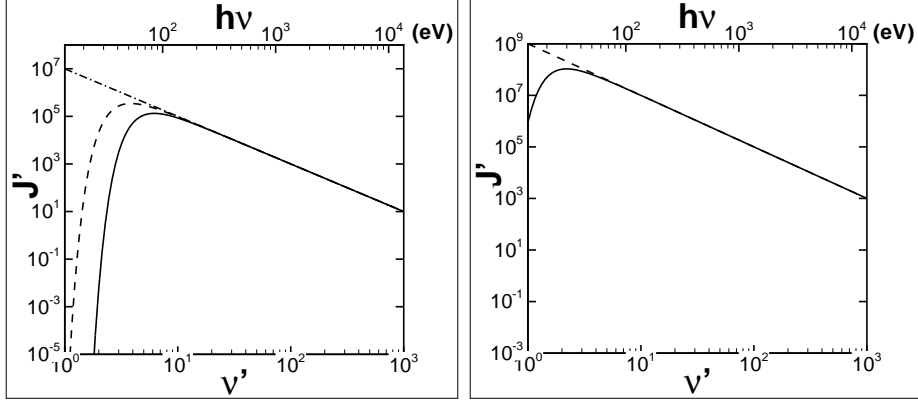


Fig. 6.  $J'(t, r, \nu)$  vs.  $\log \nu/\nu_0$  at time  $t = 0.89$  Myrs. 1.) Left panel: for the source  $\dot{E} = 5.8 \times 10^{43}$  erg s $^{-1}$ , at physical distance  $r = 0.08$  (dash dot),  $0.11$  (dash) and  $0.14$  (solid line) Mpc; and 2.) Right panel: for the source  $\dot{E} = 5.8 \times 10^{45}$  erg s $^{-1}$  at physical distance  $r = 0.19$  (dash) and  $0.24$  (solid line) Mpc. Redshift is  $1 + z = 10$ . The mesh in the numerical simulation is the same as that in Figure 3.

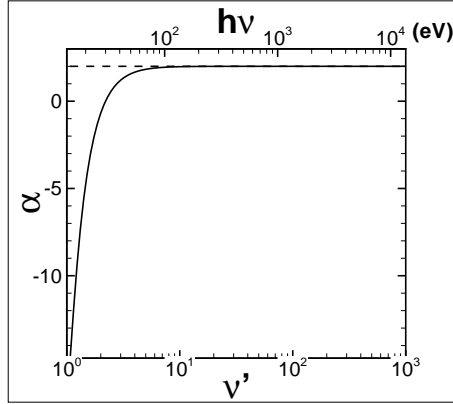


Fig. 7.  $\alpha$  vs.  $\log \nu/\nu_0$  for the source  $\dot{E} = 5.8 \times 10^{45}$  erg s $^{-1}$  at physical distance  $r = 0.19$  (dash) and  $0.24$  (solid line) Mpc. Redshift is  $1 + z = 10$ . The mesh in the numerical simulation is the same as that in Figure 3.

The spectral hardening can be measured by the index of power law defined as

$$\alpha = -\frac{\partial \ln J}{\partial \ln \nu}. \quad (32)$$

Figure 7 plots  $\alpha$  vs.  $\nu$  for the frequency spectra of Figure 6. Obviously, in the band  $\nu/\nu_0 < 10$ ,  $\alpha$  becomes smaller at larger  $r$ . Both Figures 6 and 7 show that the frequency spectra of photons depend strongly on  $t$  and  $r$  when  $t$  and  $r$  are close to or inside the pre-heating layer.

## 5 Discussions and conclusions

We have described WENO scheme which is able to solve the phase-space distribution function of photons in an isolated ionized patch around individual source in the early stage of reionization. This algorithm can produce robust results for the propagation of the I- and T-fronts. It can also give stable results for the time-dependent distribution of the small fraction of neutral hydrogen within the I-front. We have developed the method to deal with the stiffness of rate equations in time integration. Consequently, the computational speed is acceptable. This algorithm can be applied to problems with a wide range of intensity of sources, from  $10^{39}$  to  $10^{45}$  erg  $s^{-1}$  with a power law spectrum at redshift  $1 + z = 10$ . Since this algorithm treat the frequency space as well as physical space, it can also be used for sources with other frequency spectrum. We have not considered helium and secondary effects in the atomic processes yet, however the algorithm has no practical difficulty to include these factors.

We show that a common feature of the UV photon sources in the reionization epoch is to form a preheating region. In the first stage the I- and T-fronts in baryon gas are coincident, and propagate with the speed about the same as the speed of light. When the frequency spectrum of the UV photons is hardened, the evolution enters into the second stage. The propagation speeds of both the ionizing and heating fronts are less than that of light, but the T-front is always moving faster than the ionizing front. In the spherical shell between the I- and T-fronts, the kinetic temperature of gas can be as large as  $T \simeq 10^{3-4}$ , while atoms are almost neutral. Obviously, the shell would be of interest in the search for the 21 cm emission from the reionization epoch. The details of the preheating region are sensitively dependent on the parameters of the problems. For instance, the radius and thickness of the preheated shell do not show a scaling relation on their dependence of the source intensity. Therefore, an algorithm, which can properly handle models with various parameters is necessary.

Using these results, one can make comments on some numerical solvers used for the radiative transfer equations. Several solvers are based on the approximation of omitting the time-derivative term of the radiative transfer equation (Nakamoto et al. 2001; Cen 2002; Razoumov et al. 2002; Rijkhorst et al. 2005; Susa 2006). They calculate the static ionization field for a given uniform or non-uniform density fields of cosmic baryon matter. These codes essentially are generalizing the static solution eq.(1) to the case of inhomogeneous background distribution of baryon matter, and multiple sources. Such an approximation is useful to calculate the ionization field for each given inhomogeneous mass field of baryon matter, but it will no longer be a good approximation when the retardation effect due to photon propagation is important. For the problem of ionization profiles around a point source, the retardation of photon is not

always negligible. For instance, one finds the following parameters have been used in the model: the ionization and heating at comoving distance  $r = 10 \text{ h}^{-1} \text{ Mpc}$  from a point source of age  $t = 0.5 \times 10^6 \text{ yrs}$  at redshift  $z = 30$  (e.g. Cen, 2006). These parameters already violated the retardation constraint  $r \leq ct$ .

The retardation effect can be seen from the time-dependence of the I-front,  $r_I(t)$ . If the retardation effect is negligible, an analytical solution of  $r_I(t)$  is given by e.g. Whalen & Norman (2006)

$$r_I(t) = R_s [1 - e^{-t/t_{rec}}]^{1/3}, \quad (33)$$

where  $R_s = (3\dot{N}/4\pi\alpha_{\text{HII}}n_H^2)^{1/3}$  is the static radius of the Strömgen sphere given by eq.(2), and  $t_{rec} = 1/\alpha_{\text{HII}}n_H$  is recombination time scale. According to eq.(33), the time scale of the  $r_I(t)$  evolution is  $t_{rec}$ , which is independent of the source intensity  $\dot{E}$ . That is,  $r_I(t) \simeq R_s$  only if  $t \gg t_{rec}$ , regardless  $\dot{N}$ . However, Figure 4 shows that time scale of the  $r_{90}(t)$  evolution is  $\dot{N}$ -dependent. This result also holds if we replace  $r_{90}(t)$  by, e.g.  $r_{95}(t)$ , and is true for a monochromatic source too.

Considering the retardation effect, an analytical solution of  $r_I(t)$  is approximately given by the following algebraic equation (White et al. 2003)

$$r_I(t) = \left[ \frac{t - (r_I(t)/c)}{4\pi n/3\dot{N}} \right]^{1/3}. \quad (34)$$

According to eq.(34), when  $t \ll t_c = (3\dot{N}/4\pi nc^3)^{1/2}$ , the speed of the I-front,  $dr_I(t)/dt \simeq c$ , and when  $t \gg t_c$ ,  $dr_I(t)/dt \propto t^{-2/3}$ . It is qualitatively consistent with  $dr_{90}(t)/dt$  shown in Figure 4. First, the time scale of the  $r_{90}(t)$  evolution is approximately  $\propto \dot{N}^{1/2}$ , the larger the  $\dot{N}$ , the longer the  $t_c$ . Second,  $dr_I(t)/dt$  decreases with  $t$  by a power law  $dr_{90}(t)/dt \propto t^{-\beta}$  when  $t$  is large. However, the power law index  $\beta > 2/3$ . This is expected, because eq.(34) does not include the effect of recombination, which leads to a slower decrease than  $dr_{90}(t)/dt$ .

A common assumption used in eqs.(33) and (34) is that the distribution  $f_{\text{HI}}(t, r)$  is described by a step function like eq.(1). Obviously, it ignores the neutral hydrogen HI probably remained within  $r_I(t)$ . The tiny fraction of HI may also be hardly calculated well by Monte-Carlo codes (Ciardi et al. 2001; Maselli et al. 2003), which yield large numerical errors due to Poisson shot noise.

The WENO algorithm has been successfully applied to kinetic equations of the distribution function in the phase space with one or two spatial dimensions and two or three phase space dimensions with acceptable computational speed (Carrillo et al. 2006). We believe that it is not difficult to implement the WENO algorithm for radiative transfer problems with similar dimensions in the phase space.

In our calculation, the evolution the cosmic baryon gas is not tracked by the hydrodynamic equations, but is simply assumed to have a uniform distribution with density  $n$ . This treatment would be reasonable if the typical time scale of the relevant hydrodynamic effects are less than that of the I- and T-fronts. For instance, dynamical effects associated with sonic propagation would be negligible in solving the propagation of the I- and T-fronts. Of course, one can expect that richer results will be yielded if the WENO scheme for radiative transfer problems can be incorporated with the Euler hydrodynamics. Since the WENO scheme for the cosmological hydrodynamical simulation has already been well established, it would be possible to develop a unified radiation/N-body/hydrodynamics code for cosmological problems.

### Acknowledgments.

This work is supported in part by the US NSF under the grants AST-0506734 and AST-0507340. LLF acknowledges support from the National Science Foundation of China under the grant 10573036.

## A Equations of Radiative Transfer

For an ionized sphere associated with a point photon source, the radiation transfer (RT) equation is (Bernstein, 1988, Qiu et al. 2006)

$$\frac{\partial J}{\partial t} + \frac{1}{a} \frac{\partial}{\partial x^i} (n^i J) - H \left( \nu \frac{\partial J}{\partial \nu} - 3J \right) = -k_\nu J + S. \quad (\text{A.1})$$

where  $J(t, \mathbf{x}, \nu, n_i)$  is the specific intensity,  $a$  the cosmic factor,  $H = \dot{a}/a$ ,  $\nu$  the frequency of photon and  $n_i$  a unit vector in the direction of photon propagation. In eq.(A.1), we take  $c = 1$ .  $k_\nu$  and  $S$  are, respectively, the absorption and sources of photons. The absorption coefficient of eq.(A.1) is given by

$$k_\nu = \sigma(\nu) n_{\text{HI}}(t, \mathbf{x}) \quad (\text{A.2})$$

where the cross section  $\sigma(\nu) = 6.3 \times 10^{-18} (\nu_0/\nu)^3 \text{ cm}^2$ .

The number density of neutral hydrogen HI,  $n_{\text{HI}}(t, \mathbf{x})$ , is determined by

$$\frac{df_{\text{HI}}}{dt} = \alpha_{\text{HII}} n_e f_{\text{HII}} - \Gamma_{\gamma\text{HI}} f_{\text{HI}} - \Gamma_{\text{eHI}} n_e f_{\text{HI}}, \quad (\text{A.3})$$

Relevant parameters are taken from Theuns et al. (1998) as

1. recombination coefficient

$$\alpha_{\text{HII}} = 6.30 \times 10^{-11} T^{-1/2} T_3^{-0.2} / (1 + T_6^{0.7}), \quad (\text{A.4})$$

where  $T$  is temperature, and  $T_n = T/10^n$ .

2. collision ionization

$$\Gamma_{\text{eHI}} = 1.17 \times 10^{-10} T^{1/2} e^{-157809.1/T} (1 + T_5^{1/2})^{-1} \quad (\text{A.5})$$

3. photoionization

$$\Gamma_{\gamma\text{HI}}(t, r) = \int_{\nu_0}^{\infty} d\nu \frac{J(t, r, \nu)}{h\nu} \sigma(\nu). \quad (\text{A.6})$$

The temperature  $T$  is determined by the equation

$$nk_{\text{B}} \frac{dT}{dt} = H - n^2 C. \quad (\text{A.7})$$

4. heating rate

$$H = n_{\text{HI}} \int_{\nu_0}^{\infty} d\nu J(t, r, \nu) \sigma(\nu) \frac{\nu - \nu_0}{\nu} \quad (\text{A.8})$$

where  $h\nu_0 = 2.176 \times 10^{-11}$  ergs.

5. cooling. Since only the recombination cooling is important, we have

$$\begin{aligned} C = & 8.70 \times 10^{-27} T^{1/2} T_3^{-0.2} (1 + T_6^{0.7})^{-1} [1 - f_{\text{HI}}]^2 \\ & + 1.42 \times 10^{-27} T^{1/2} [1 - f_{\text{HI}}]^2 \\ & + 2.45 \times 10^{-21} T^{1/2} e^{-157809.1/T} (1 + T_5^{1/2})^{-1} (1 - f_{\text{HI}}) f_{\text{HI}} \\ & + 7.5 \times 10^{-19} e^{-118348/T} (1 + T_5^{1/2})^{-1} (1 - f_{\text{HI}}) f_{\text{HI}} \end{aligned} \quad (\text{A.9})$$

where  $T_n = T/10^n$ . The terms on the r.h.s. of eq.(A.9) are, respectively, the recombination cooling, collisional ionization cooling, collisional excitation cooling and bremsstrahlung. Both  $H$  and  $C$  are in the unit of ergs  $\text{cm}^3 \text{s}^{-1}$ .

## References

- [1] Alvarez, M., Bromm, V. & Shpiro, P. 2006, ApJ, 639, 621
- [2] Bernstein, J., 1988, Kinetic Theory in the Expanding Universe, Cambridge
- [3] Carrillo, J., Gamba, I., Majorana, A. & Shu, C.-W., 2006, J. Comp. Phys., 214, 55
- [4] Cen, R., 2002, ApJS, 141, 211
- [5] Cen, R., 2006, ApJ, 648, 47
- [6] Cen, R. & Haiman, Z., 2000, ApJL, 542, L75
- [7] Chen, X & Miralda-Escudé, J., 2006, astr-ph/0605439

- [8] Ciardi, B., Ferrara, A., Marri, S., & Raimondo, G. 2001, MNRAS, 324, 381
- [9] Feng, L.L., Shu, C.-W., & Zhang, M.P., 2004, ApJ, 612, 1
- [10] Gnedin, N.Y. & Abel, T., 2001, NewA, 6, 437
- [11] Iliev, I.T. et al. 2006, MNRAS, 371, 1057
- [12] Jiang, G. & Shu, C.-W., 1996, J. Comp. Phys., 126, 202
- [13] Kitayama, T., Yoshida, N., Susa, H. & Umemura, M., 2004, ApJ, 613, 631
- [14] Madau, P. & Rees, M., 2000, ApJL, 542, L69
- [15] Maselli, A., Ferrara, A. & Ciardi, B. 2003, MNRAS, 345, 397
- [16] Mellema, G., Iliev, I.T., Alvarez, M.A. & Shapiro, P.R. 2006, NewA, 11, 374
- [17] Nakamotoi, T., Umemura, M. & Susa, H. 2001, MNRAS, 321, 593
- [18] Osterbrock, D. & Ferland, G. 2005, Astrophysics of Gaseous Nebulae and Active Galactic Nuclei, (University Science Books)
- [19] Qiu, J.-M., Shu, C.-W., Feng, L.-L. & Fang, L.Z., 2006, NewA, 12, 1
- [20] Razoumov, A., Norman M., Abel, T. & Scott, D. 2002, ApJ, 572, 695
- [21] Razoumov, A. & Scott, D. 1999, MNRAS, 309, 287
- [22] Ricotti, M., Gnedin, N., Shull, J. 2002, ApJ, 575, 33
- [23] Rijkhorst, E., Plewa, T., Dubey, A. & Mellema, G. 2005, astr-ph/0505213
- [24] Shapiro, P.R., Iliev, I.T. & Raga, A.C. 2004, MNRAS, 348, 753
- [25] Shu, C.-W., 2003, Int. J. Comp. Fluid Dyn., 17, 107
- [26] Shu, C.-W. & Osher, S., 1988, J. Comp. Phys., 77, 439
- [27] Sokasian, A. Abel, T. & Hernquist, L.E. 2001, NewA, 6, 359
- [28] Strömgren, B., 1939, ApJ, 89, 529
- [29] Susa, H. 2006, Pub. Astron. Soc. Japan. 2006, 58, 445
- [30] Theuns, T., Leonard, A., Efstathiou, G., Pearce, F.R. & Thomas, P.A., 1998, MNRAS, 301, 478
- [31] Tozzi, P., Madau, P., Meiksin, A. & Rees, M. 2000, ApJ, 528, 597.
- [32] Whalen, D. Abel, T., & Norman, M. 2004, ApJ, 610, 14
- [33] Whalen, D. & Norman, M. 2006, ApJS, 162, 281
- [34] White, R.L., Becker, R.H. & Fan, X.H. 2003, ApJ, 126, 1
- [35] Wyithe, J., Loeb, A., 2004, Nature, 427, 815
- [36] Wyithe, J. & Loeb, A. & Barnes, D., 2005, ApJ, 634, 715
- [37] Xu, Z. & Shu, C.-W., 2005, J. Comp. Phys., 205, 458
- [38] Yu, Q.J., 2005, ApJ, 623, 683
- [39] Yu, Q.J., & Lu, Y.J., 2005, ApJ, 621, 31